IEEE Photonics Journal
An IEEE Photonics Society Publication

Open Access

Image Plane Holographic Microscopy With a Table-Top Soft X-Ray Laser

Volume 7, Number 1, February 2015

J. Nejdl
I. D. Howlett
D. Carlton
E. H. Anderson
W. Chao
M. C. Marconi, Fellow, IEEE
J. J. Rocca, Fellow, IEEE
C. S. Menoni, Fellow, IEEE

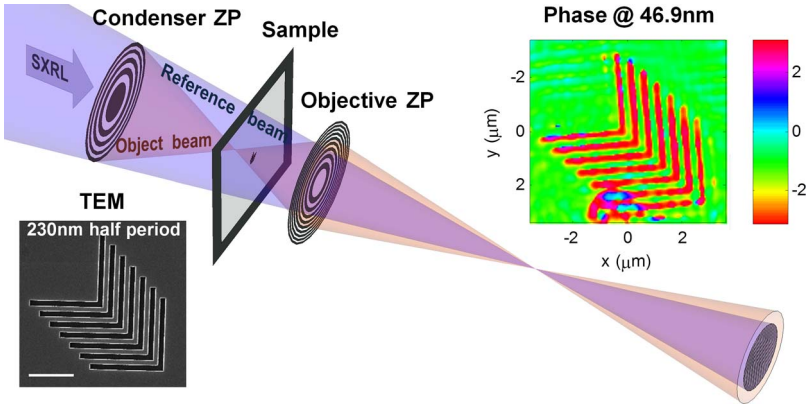

DOI: 10.1109/JPHOT.2015.2389957
1943-0655

IEEE photonics SOCIETY

IEEE

Image Plane Holographic Microscopy With a Table-Top Soft X-Ray Laser

J. Nejdl,[1,4,5] I. D. Howlett,[1,2] D. Carlton,[3] E. H. Anderson,[3] W. Chao,[3] M. C. Marconi,[1,2] *Fellow, IEEE*, J. J. Rocca,[1,2] *Fellow, IEEE*, and C. S. Menoni,[1,2] *Fellow, IEEE*

[1]National Science Foundation Engineering Research Center for Extreme Ultraviolet Science and Technology, Fort Collins, CO 80523-1320 USA
[2]Department of Electrical and Computer Engineering, Colorado State University, Fort Collins, CO 80523-1373 USA
[3]Center for X-Ray Optics, Lawrence Berkeley National Laboratory, Berkeley, CA 94720 USA
[4]Institute of Physics of ASCR, ELI Beamlines Project, 182 21 Prague, Czech Republic
[5]Faculty of Nuclear Sciences and Physical Engineering (FNSPE), Czech Technical University in Prague, 166 36 Prague, Czech Republic

DOI: 10.1109/JPHOT.2015.2389957

Manuscript received November 12, 2014; accepted November 14, 2014. Date of publication January 13, 2015; date of current version February 18, 2015. This work was supported by the National Science Foundation (NSF) under Award EEC-0310717 using equipment developed under NSF Award MRI-ARRA 09-561. The work of J. Nejdl was supported in part by the Fulbright Program and by the Ministry of Education, Youth, and Sport of the Czech Republic under Project ECOP CZ.1.07/2.3.00/20.0279, Project CZ.1.07/2.3.00/30.0057, and Project ELI-Beamlines CZ.1.05/1.1.00/02.0061. Corresponding author: C. S. Menoni (e-mail: Carmen.Menoni@colostate.edu).

Abstract: We demonstrate image plane holographic microscopy in the soft X-ray (SXR) spectral region, combining the coherent output from a 46.9-nm wavelength table-top SXR laser and two Fresnel zone plates. Phase and amplitude maps of the object are simultaneously obtained from holograms created at the image plane by the superposition of a reference and object beam originating from the zero and first diffraction order of the zone plates. We have used the microscope to record holograms of nanometer-scale periodic Si elbow patterns with ~30% absorption contrast at the laser wavelength. The measured phase shift of 2.3 rad accurately predicts the Si dense line step height of 100 nm. The scheme is scalable to shorter wavelengths and allows for simultaneous high spatial and temporal resolution.

Index Terms: Holography, EUV, X-ray imaging, extreme ultraviolet and X-ray lasers.

1. Introduction

The use of phase contrast in microscopy to observe transparent objects, which is an old concept devised by Zernike, has spurred the development of imaging methods that are capable of quantitatively measuring phase changes across the field of view of an image [1]. Phase information can be converted to variations in refractive index or density if the thickness of the sample is known. Quantitative phase imaging is widely exploited for biological imaging at optical wavelengths where natural absorption contrast is essentially absent [2]–[4].

Quantitative measurements of both phase and amplitude of a wave can be obtained with digital holographic imaging and with quantitative phase imaging [5]–[7]. In holography, the object wave is benchmarked with a reference beam while in quantitative phase imaging it is the imaging field [6]. A particular holographic configuration is Image Plane Digital Holographic Microscopy

(IPDHM) [7]. The implementation of IPDHM requires splitting a coherent beam into a reference beam and a second beam that illuminates the object. An image of the object is formed by an objective lens at the detector plane where this "object wave" is made to interfere with the reference beam creating a hologram. Analysis of the resulting interference pattern allows for the quantitative evaluation of the phase and amplitude of the object wave on every pixel across the image.

IPDHM using visible illumination has been applied to image stain-free biological samples that have extremely low absorption contrast at optical wavelengths [2], [3], [8]. Imaging at extreme ultraviolet (EUV) and soft X-ray (SXR) wavelengths also suffers from lack of absorption contrast when the EUV/SXR photon energy does not coincide with atomic resonances of the sample's materials [9]. Nevertheless EUV and SXR can provide very high sensitivity in assessing phase shifts [10]. This coupled with the tens of nanometer lateral resolution of EUV/SXR microscopes [11] makes it possible to obtain 3-D images of nanoscale objects. Different EUV/SXR imaging methods that exploit phase contrast have been demonstrated. Zernike phase contrast microscopy was initially demonstrated by incorporating a phase plate at the objective back focal plane [10]. The concept was later elegantly refined by combining the zone plate objective and phase mask into a single diffractive optical element [12], [13]. However, this imaging modality is not quantitative. Zone plates have also been used in SXR interferometry and Fourier holography to generate the reference beam [14]–[18].

Herein, we describe the demonstration of IPDHM at SXR wavelengths in an experiment designed to simultaneously obtain quantitative phase and amplitude maps of a sample with high spatial resolution. The microscope uses two zone plates that when illuminated by a converging SXR laser beam generate reference and object waves that interfere at the detector plane. Interferograms of a weakly absorbing sample consisting of Si elbow patterns with periods down to 150 nm, defined on a silicon nitride membrane were obtained. Reconstruction of the image plane holograms allowed us to obtain phase maps from which nanometer-scale variations in the thickness across the sample could be determined.

2. Experimental Design

In the SXR IPDHM microscope a converging beam illuminates a condenser zone plate (CZP) that acts as both beam splitter and focusing element. The CZP zero diffraction order serves as the reference beam and its first diffraction order creates the object beam that illuminates the sample. A second zone plate, i.e., the objective zone plate (OZP), creates a magnified image of the object that is made to interfere with the reference beam at the image plane to create the hologram. The conceptual design and the coherence demands of this microscope were previously discussed [19]. Fig. 1 shows the OZP focuses the object beam in the vicinity of the focus of the reference beam which passes unaffected through the CZP and OZP. This configuration ensures both the efficient illumination of the sample and the same wavefront curvature for the reference and object waves at the detector plane while minimizing the limitations imposed by the temporal coherence of the illumination. The sample is placed near the first order focus of the CZP and its image is formed by the first diffraction order of the OZP at the detector plane. The interference between the object and reference waves gives rise to a fringe pattern that is captured by a back-illuminated X-ray charged coupled device array detector. The fringe spacing and fringe orientation in the image-plane hologram are controlled by displacing the position of the object beam focus with respect to the focus of the reference beam on a plane perpendicular to the optical axis. In this geometry, it is possible to obtain in-line holograms (reference and object waves are concentric), or off-axis holograms with adjustable fringe spacing that is constrained by the overlap of the reference and object beams.

Generally, the object beam at the image plane is a shifted point-symmetrical copy of the reference beam. That is why the spatial coherence of the illuminating beam is a critical issue in the experimental design. We have analyzed the coherence demands of the illumination for the SXR IPDHM microscope geometry shown in Fig. 1 [19]. This analysis showed the distance c between the CZP and the focus of the reference beam, the distance d between CZP and OZP and

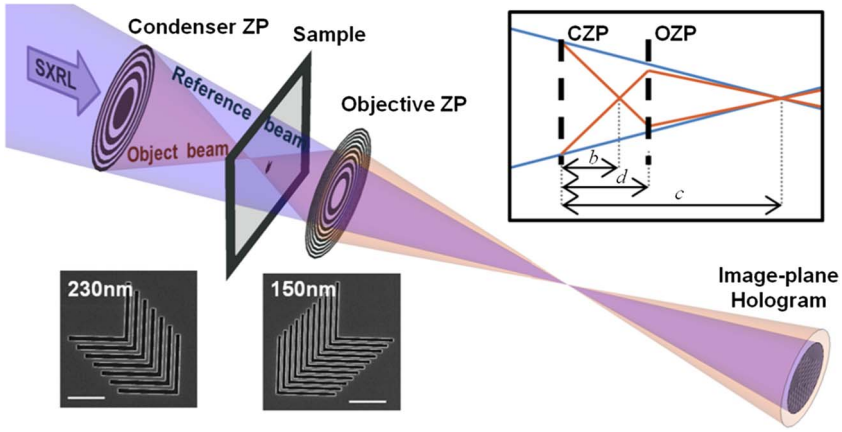

Fig. 1. Schematic of the two zone plate IPDHM setup. The reference and object beams are colored purple and orange, respectively. Scanning electron micrographs of test samples consisting of dense Si lines with 230 nm and 150 nm linewidth arranged on an elbow pattern are shown. The white scale bar corresponds to 2 μm. The top right inset depicts the notation of the positions of the zone plates with respect to the reference beam focus.

distance b between the CZP and its first order focus are related to the OZP first order focal length f_{ozp} via the thin lens equation as

$$\frac{1}{d-b}+\frac{1}{c-d}=\frac{1}{f_{ozp}} \Rightarrow d=\frac{c+b-\sqrt{(c-b)(c-b-4f_{ozp})}}{2}. \tag{1}$$

The solution to (1) that results in the smaller d is chosen to obtain an image of the sample with high magnification and at the same time to ensure that the reference beam is significantly expanded at the sample plane. Finally, the sample and detector positions can be found from the required magnification following the thin lens equation for the OZP.

One can also evaluate the intensity ratio of the reference and the object beam at the image plane as

$$\frac{I_r}{I_o}=\frac{\eta_0^2}{\eta_1^2}\left[\frac{c(d-b)}{b(c-d)}\right]^2 \tag{2}$$

with η_m denoting the mth-order far field diffraction efficiency of the zone plates. From this ratio the maximum fringe visibility (for the case of fully coherent beam) can be calculated as

$$V:=\frac{I_{max}-I_{min}}{I_{max}+I_{min}}=\frac{2\sqrt{I_rI_o}}{I_r+I_o}=2\frac{\sqrt{I_r/I_o}}{I_r/I_o+1}. \tag{3}$$

Notice that the maximum fringe visibility is independent of the magnification of the imaging setup.

3. Experimental Setup

Our implementation of SXR IPDHM (see Fig. 1) is based on a modification of a compact full field SXR microscope that has been used to image nanostructures and nanoscale dynamics with ~50 nm lateral spatial resolution [20], [21]. The SXR IPDHM setup used as illumination the output from a Ne-like Ar capillary discharge laser delivering pulses of ~0.1 mJ energy, 1.2 ns duration at a wavelength of 46.9 nm [22], [23]. The laser output illuminates a Schwarzschild condenser placed 1.5 m downstream. This optical element consists of two spherical mirrors coated with Sc/Si multilayers each with 40% reflectivity [24]. Its effective focal length is 27 mm, and its numerical aperture is 0.18 NA. The Schwarzschild condenser creates a converging

TABLE 1

Parameters of the configurations used for the experiment

	Setup 1	Setup 2
CZP diameter D	0.5 mm	
CZP focal length f_{czp}	2.13 mm	
CZP Numerical aperture NA_{czp}	0.12	
OZP diameter	0.5 mm	
OZP focal length f_{ozp}	1.07 mm	0.48 mm
OZP Numerical aperture NA_{ozp}	0.23	0.46
Distance between ref. beam focus and CZP c	22.5 mm	16.9 mm
Distance between CZP and OZP d	3.07 mm	2.39 mm
Diameter of the object beam at the sample plane	15 μm	4 μm
Magnification	600	900

spherical wave with low aberrations. A fraction of this beam illuminates a 0.5 mm diameter CZP of numerical aperture 0.12 NA and first order focal length of 2.13 mm. We used two OZPs with the same diameter, 0.5 mm, and numerical apertures of 0.23 NA and 0.46 NA to achieve magnifications of 600× and 900×, respectively. All the zone plates employed in our experiment were free standing Ni binary amplitude Fresnel zone plates with diffraction efficiencies $\eta_0 \approx 0.25$ and $\eta_1 \approx 0.1$ for the zero and first order, respectively. This zone plate arrangement results in a maximum energy throughput of 1% for the object beam and 6% for the reference beam not including sample losses. The geometrical parameters of both configurations are listed in Table 1.

To ensure the CZP was illuminated by a fully spatially coherent beam to achieve maximum fringe visibility, the length of the capillary laser gain medium was selected to be 26 cm resulting in coherence area radius of 135 μm at 40 cm from the source [25]. It is important to point out that since the laser output is highly monochromatic, $\Delta\lambda/\lambda \approx 4 \times 10^{-5}$, which is equivalent to the coherence length of ~700 μm [26], the fringe visibility is practically unaffected. Due to the common-path nature of the setup the maximum ray path-length difference is below 30 μm for either of the imaging configurations [27].

The sample consisted of a set of dense Si lines forming an elbow grating with linewidths of 150 and 230 nm (see inset in Fig. 1) fabricated by electron beam lithography [28]. Upon processing, 100 nm tall Si elbows were defined within a region 20×20 μm^2 on the 0.5 mm × 0.5 mm, 30 nm thick, silicon nitride window. This design allowed for the reference beam to propagate through the sample with minimum distortion.

4. Results

Off-axis image plane holograms were obtained with typical exposures of 5-30 laser shots with the laser operating at 2 Hz repetition rate to obtain a reasonable signal-to-noise-ratio (SNR > 20). The fringe spacing of the holograms was set to 11 and 8 pixels when using the 0.23 NA and 0.46 NA OZP respectively. This ensured maximum overlap of the reference and object beam without compromising field of view. Following the acquisition of each holographic image, a reference hologram image was acquired by removing the sample. This allowed for subtraction of beam in-homogeneities, which in turn, contributed to enhance the quality of the reconstructed amplitude and phase images.

The off-axis holograms were analyzed using a Fourier transform method which consisted of applying a point-symmetrical band-pass filter centered at the carrier frequency (spatial frequency of interference fringes) to extract the complex field of the object wave, i.e., its phase and amplitude [29]. The boundary of the frequency filter was set to the theoretical on-axis resolution of the system to eliminate noise originating from unresolved frequencies. A hologram of a 230 nm half period Si elbow pattern acquired using the OZP with numerical aperture 0.23 NA and magnification 600× is shown in Fig. 2(a).

From the reconstruction of this hologram the phase and amplitude images shown in Fig. 2(b) and (c) were obtained. The circular pattern at the bottom of the phase map [see Fig. 2(b)] is

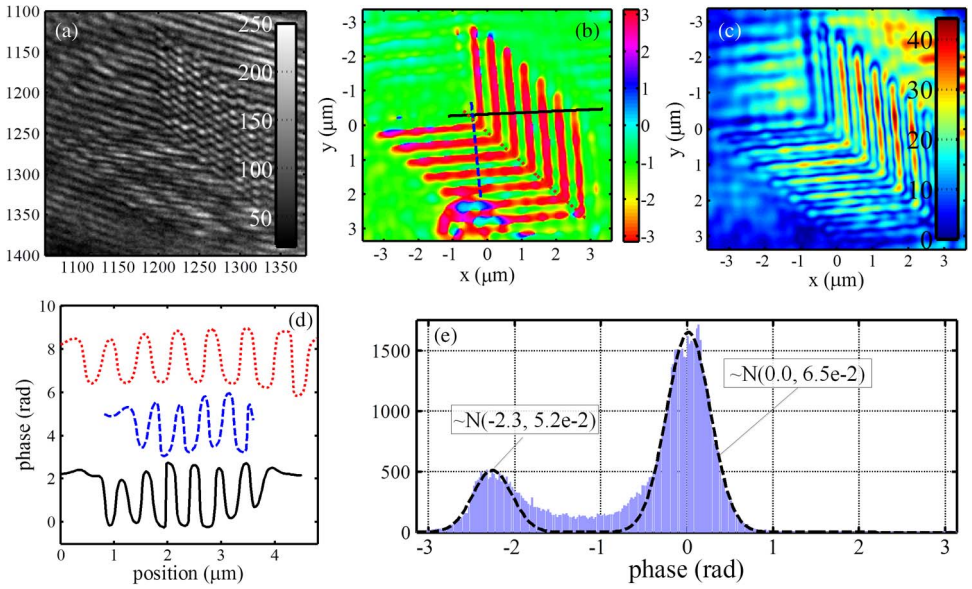

Fig. 2. (a) Image plane hologram of the Si elbow pattern with dense 230 nm lines recorded with the 0.23 NA OZP. From its reconstruction, maps of the phase shift (b) and amplitude (c) of the object wave were obtained. The bar insets are intensity, absolute phase, and amplitude, respectively. (d) Lineouts showing the phase shift modulation along the horizontal (solid black line), vertical (dashed blue line), and diagonal (dotted red line) in the phase image (b). Different plots are offset in phase by π and 2π for clarity. (e) Histogram of the phase map of (b) showing a phase shift of (2.3 ± 0.3) rad between the peaks and valleys. The dashed line in (e) represents weighted normal distribution fits with mean and variance values indicated in the figure.

caused by inhomogeneity of the object beam resulting from using a CZP with a central opening. The phase map of Fig. 2(b) was analyzed to extract the mean phase shift. The histogram of the phase within a 40 μm^2 field of view of the image (excluding the circular pattern) is shown in Fig. 2(e). A fit of the histogram with Gaussian functions, allowed us to extract a phase difference of $\Delta\Phi = (2.3 \pm 0.3)$ rad which corresponds to a Si thickness of $\Delta d = (100 \pm 15)$ nm when using the tabulated refractive index of Si, $\tilde{n} = 0.83 - 0.012i$ [30] in the relation

$$\Delta\Phi = \frac{2\pi}{\lambda}(n-1)\Delta d \tag{4}$$

with λ denoting the wavelength of the illumination and n the real part of the refractive index $\tilde{n}$. This result is in good agreement with the thickness specifications of the sample.

Images of the 150 nm half period Si elbow pattern were obtained with a magnification of 900$\times$ using the 0.46 NA OZP. The recorded hologram and the corresponding phase and amplitude maps are shown in Fig. 3(a)–(c), respectively. From the analysis of the phase image, a phase shift $\Delta\Phi = (2.9 \pm 0.6)$ rad is obtained. This case shows a larger spread in the phase compared with the results of Fig. 2. This is in part due to a reduction in fringe visibility resulting from a decrease in the signal level when using higher magnification and the smaller coherence area of the illumination at the CZP location which at higher magnification is closer to the reference beam focus. The aberrations of this high-NA zone plate might have also contributed to the lower quality of the hologram.

5. Discussion

The IPDHM quantitatively determines the object wave electric field phasor at the image plane. Therefore, analysis of its spatial resolution with a classical two-point resolution criterion or a knife-edge method is not applicable. Nevertheless, it is possible to analyze which are the factors that lead to errors in the determination of the electric field phasor. In IPDHM, the quantitative

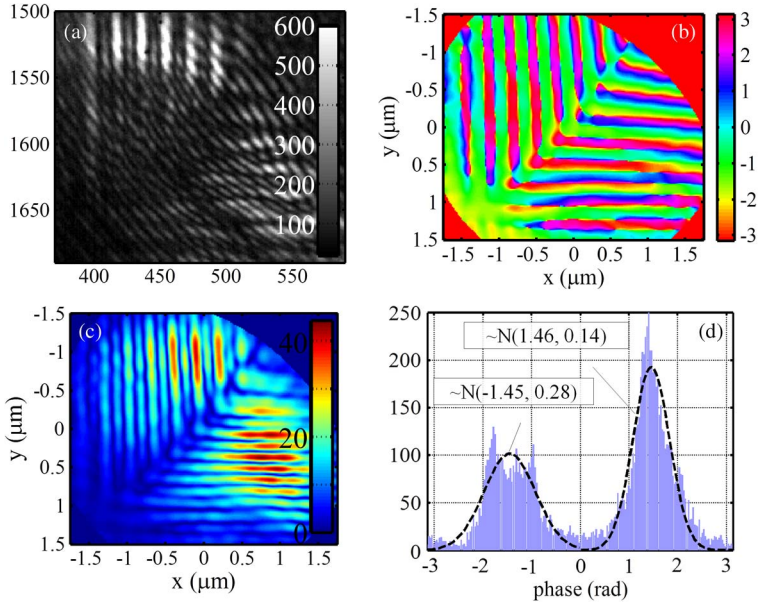

Fig. 3. Hologram of the Si sample with dense 150 nm lines recorded with the 0.46 NA OZP. (a) Recorded hologram, (b) phase, (c) amplitude, and (d) histogram of the phase. The phase shift calculated from the phase image equals (2.9 ± 0.6) rad. The dashed line in (d) represents weighted normal distribution fits with mean and variance values indicated in the figure.

determination of the phasor requires both center-symmetric components of a given spatial frequency (its $+1$ and -1 diffraction orders) to be transferred by the OZP. We can define the cut-off frequency of the optical system as the maximum spatial frequency that satisfies this condition, so the phasor of the electric field can be evaluated correctly. For an extended object, the cut-off frequencies transferred by the system equal NA_{ozp}/λ near the optical axis and reduce linearly over the field of view to $(NA_{ozp} - NA_{czp})/\lambda$ on the periphery of the object beam which is divergent on the sample plane (see Fig. 1). We can write the cut-off frequency of a region in the object beam as a function of its distance from the center of the object beam r as

$$\xi_{cutoff}(r) = \frac{1}{\lambda}\left(NA_{ozp} - \frac{r}{R}NA_{czp}\right), \qquad r \in [0, R] \tag{5}$$

where R denotes the radius of the object beam at the sample plane. As shown by (5), when imaging an extended object that covers a substantial region of the object beam, as occurs in our case when using the highest magnification (see Fig. 3), the spatial resolution of the measurements is reduced. For the OZPs with NA $= 0.23$ and NA $= 0.46$ the cut-off frequencies are 4.9 μm^{-1} and 9.8 μm^{-1} on the optical axis and reduce to 2.3 μm^{-1} and 7.2 μm^{-1} on the periphery of the field of view, respectively. Assuming an aberration free system the two configurations should be able to resolve 210 nm and 70 nm half-period structures over the entire field of view, respectively. In addition, the limited numerical aperture contributes to the error in the phase shown as a spread around the central peaks in the histograms. This is because due to the geometry of the dense line Si elbow gratings only spatial frequencies that are odd multiples of the fundamental frequency are present. The third harmonics have spatial frequencies of 6.5 μm^{-1} and 10 μm^{-1} which exceed the cut-off frequency of the 0.23 NA and 0.46 NA OZP, respectively. Therefore, only the fundamental frequency is transferred and the phase maps extracted from the holograms exhibit a sinusoidal profile instead of a step-wise pattern as seen from the phase cuts in Fig. 2(d).

The quality of the holograms is affected by the degree of coherence of the illumination. A detailed ray tracing analysis has shown low demands on temporal coherence that are easily met by the SXR laser, but significant requirements on spatial coherence that constrain the design of

the experimental setup, as discussed briefly in Section 2 and more extensively in [19]. Notice that the limited extension of the coherence area limits the field of view, but it does not affect the spatial resolution of the method, as the hologram is recorded in the image plane. Improving the spatial coherence of the illumination while preserving the photon flux would lead to an increased field of view of the microscope. This could be accomplished by increasing the gain length of the capillary discharge laser.

The quality of the holograms, and hence the accuracy in the determination of the phase and amplitude components of the object wave electric field, can also be affected by other factors. The contributions of the different diffraction orders of the zone plates affect the homogeneity of the reference and object beams. In the experimental design we considered only the zero diffraction order of both zone plates for the reference beam and their first diffraction order for the object beam. Other orders can, however, also contribute to the total electric field at the image plane. These can be considered as a set of beams originating from point sources that lie close to the optical axis at different distances with respect to the hologram plane and thus create a radial structure on the reference and object beams at the image plane. The contribution of these diffraction orders is more important in the IPDHM geometry than in a classical zone plate microscope, because the image plane hologram is the superposition of the electric field distributions of the reference and object waves. In the case of binary amplitude Fresnel zone plates, the field diffraction efficiency scales as $1/m$, where m is an odd diffraction order [9]. The contribution of these parasitic beams is, however, reduced by their high divergence that further reduces their field amplitude at the hologram plane. Our calculations showed that the amplitude of these waves is always at least an order of magnitude lower than the field of the reference or object waves [27].

6. Conclusion

In summary, the SXR IPDHM microscope successfully obtained quantitative phase and amplitude maps of low absorbing Si dense lines with linewidth as small as 150 nm without the use of phase retrieval methods. The method could also be adapted to image in a reflection configuration. Moreover, this SXR IPDHM geometry is scalable to shorter wavelengths using the coherent and highly monochromatic output from laser-pumped SXR lasers [31], [32]. The shorter wavelength of these state-of-the-art lasers should improve resolution and enable probing of thicker samples. Additionally, the common-path nature of the method which significantly reduces the demands on the temporal coherence of the illumination coupled with the high flux of SXR lasers will allow for single-shot image plane holography with high spatial and temporal resolution. The ability to quantify phase shifts and hence optical path lengths provides a path to assess variations in density or thickness of samples at the nanoscale.

Authors' Contributions

The concept of the method was proposed by J. N. and I. D. H. The experiment was designed by J. N., I. D. H., C. S. M., J. J. R., and M. C. M. The experiment was set and realized by J. N. and I. D. H. The zone plates and samples were fabricated by D. C., E. H. A., and W. C. Treatment of the experimental data was performed by J. N. This paper was written by J. N., C. S. M., J. J. R., and M. C. M. and was proofread by all authors.

References

[1] F. Zernike, “Phase contrast, A new method for the microscopic observation of transparent objects,” *Physica*, vol. 9, no. 10, pp. 686–698, Dec. 1942.
[2] V. Chhaniwal, A. S. G. Singh, R. A. Leitgeb, B. Javidi, and A. Anand, “Quantitative phase-contrast imaging with compact digital holographic microscope employing Lloyd's mirror,” *Opt. Lett.*, vol. 37, no. 24, pp. 5127–5129, Dec. 2012.
[3] P. Marquet, C. Depeursinge, and P. J. Magistretti, “Exploring neural cell dynamics with digital holographic microscopy,” *Annu. Rev. Biomed. Eng.*, vol. 15, pp. 407–431, Jul. 2013.
[4] T. Kim, R. Zhou, L. L. Goddard, and G. Popescu, “Quantitative phase imaging: Metrology meets biology,” *Photon. J.*, vol. 6, no. 2, pp. 1–9, Apr. 2012.
[5] M. K. Kim, *Digital Holographic Microscopy: Principles, Techniques, and Applications*. New York, NY, USA: Springer-Verlag, 2011.

[6] B. Bhaduri *et al.*, "Diffraction phase microscopy: Principles and applications in materials and life sciences," *Adv. Opt. Photon.*, vol. 6, no. 1, pp. 57–119, Mar. 2014.
[7] E. Marquardt and J. Richter, "Digital image holography," *Opt. Eng.*, vol. 37, no. 5, pp. 1514–1519, May 1998.
[8] F. Yi, I. Moon, B. Javidi, D. Boss, and P. Marquet, "Automated segmentation of multiple red blood cells with digital holographic microscopy," *J. Biomed. Opt.*, vol. 18, no. 2, Feb. 2013, Art. ID. 026006.
[9] D. T. Attwood, *Soft X-Ray and Extreme Ultraviolet Radiation: Principles and Applications*. Cambridge, U.K.: Cambridge Univ. Press, 2000.
[10] G. Schmahl *et al.*, "Phase contrast studies of biological specimens with the X-ray microscope at BESSY," *Rev. Sci. Instrum.*, vol. 66, no. 2, pp. 1282–1286, Feb. 1995.
[11] W. Chao *et al.*, "Real space soft X-ray imaging at 10 nm spatial resolution" *Opt. Exp.*, 20, no. 9, pp. 9777–9783, Apr. 2012.
[12] M. C. Bertilson *et al.*, "Compact high-resolution differential interference contrast soft X-ray microscopy," *Appl. Phys. Lett.*, vol. 92, no. 6, Feb. 2008, Art. ID. 064104.
[13] A. Sakdinawat and Y. W. Liu, "Phase contrast soft X-ray microscopy using Zernike zone plates," *Opt. Exp.*, vol. 16, no. 3, pp. 1559–1564, Feb. 2008.
[14] T. Wilhein, B. Kaulich, and J. Susini, "Two zone plate interference contrast microscopy at 4 keV photon energy," *Opt. Commun.*, vol. 193, no. 1–6, pp. 19–26, Jun. 2001.
[15] M. Wieland, T. Wilhein, C. Spielmann, and U. Kleineberg, "Zone-plate interferometry at 13 nm wavelength," *Appl. Phys. B*, vol. 76, no. 8, pp. 885–889, Jun. 2003.
[16] I. McNulty *et al.*, "High-resolution imaging by Fourier transform X-ray holography," *Science*, vol. 256, no. 5059, pp. 1009–1012, May 1992.
[17] E. B. Malm *et al.*, "Tabletop single-shot extreme ultraviolet Fourier transform holography of an extended object," *Opt. Exp.*, 21, no. 8 pp. 9959–9966, Apr. 2013.
[18] D. Stickler *et al.*, "Soft X-ray holographic microscopy," *Appl. Phys. Lett.*, vol. 96, no. 4, Jan. 2010, Art. ID. 042501.
[19] J. Nejdl *et al.*, "Analysis of spatial resolution and coherence demands in soft X-ray image-plane holographic microscopy with two zone plates," *Proc. SPIE*, 2013, vol. 8849, Art. ID. 884933.
[20] C. A. Brewer *et al.*, "Single-shot extreme ultraviolet laser imaging of nanostructures with wavelength resolution," *Opt. Lett.*, vol. 33, no. 5, pp. 518–520, Mar. 2008.
[21] S. Carbajo *et al.*, "Sequential single-shot imaging of nanoscale dynamic interactions with a table-top soft X-ray laser," *Opt. Lett.*, vol. 37, no. 14, pp. 2994–2996, Jul. 2012.
[22] B. R. Benware, C. D. Macchietto, C. H. Moreno, and J. J. Rocca, "Demonstration of a high average power tabletop soft X-Ray laser," *Phys. Rev. Lett.*, vol. 81, no. 26, pp. 5804–5807, May 1998.
[23] C. D. Macchietto, B. R. Benware, and J. J. Rocca, "Generation of millijoule-level soft-X-ray laser pulses at a 4-Hz repetition rate in a highly saturated tabletop capillary discharge amplifier," *Opt. Lett.*, vol. 24, no. 16, pp. 1115–1117, Aug. 1999.
[24] I. A. Artioukov and K. M. Krymski, "Schwarzschild objective for soft X-rays," *Opt. Eng.*, vol. 39, no. 8, pp. 2163–2170, Aug. 2000.
[25] Y. Liu *et al.*, "Achievement of essentially full spatial coherence in a high-average-power soft-X-ray laser," *Phys. Rev. A*, vol. 63, no. 3, Feb. 2001, Art. ID. 033802.
[26] L. Urbanski *et al.*, "Spectral linewidth of a Ne-like Ar capillary discharge soft-X-ray laser and its dependence on amplification beyond gain saturation," *Phys. Rev. A*, vol. 85, Mar. 2012, Art. ID. 033837.
[27] J. Nejdl, "Plasma-based X-ray lasers and their applications in probing matter," Ph.D. dissertation, Czech Techn. Univ., Prague, Czech Republic, 2012, unpublished.
[28] E. H. Anderson, "Specialized electron beam nanolithography for EUV and X-ray diffractive optics," *IEEE J. Quantum Electron.*, vol. 42, no. 1, pp. 27–35, Jan. 2006.
[29] M. Takeda, H. Ina, and S. Kobayashi, "Fourier-transform method of fringe-pattern analysis for computer-based topography and interferometry," *J. Opt. Soc. Amer.*, vol. 72, no. 1, pp. 156–160, Jan. 1982.
[30] D. E. Cullen, J. H. Hubbell, and L. Kissel, "EPDL97: The evaluated photon data library," Lawrence Livermore Nat. Lab., Livermore, CA, USA, Rep. UCRL-50400, 1997.
[31] D. Alessi *et al.*, "Gain-saturated 10.9 nm tabletop laser operating at 1 Hz repetition rate," *Opt. Lett.*, vol. 35, no. 35, pp. 414–416, Feb. 2010.
[32] D. Alessi *et al.*, "Efficient excitation of gain-saturated sub-9-nm-wavelength tabletop soft-X-ray lasers and lasing down to 7.36 nm," *Phys. Rev. X*, 1, no. 2, Dec. 2011, Art. ID. 021023.